Detection and Validation of Cloud Top Height From Scanning Ka-Band Radar Measurements Using Digital Image Processing Technique

Subrata Kumar Das [ID], Pranjal Prasad Joshi, Rohit Satish Kokitkar, Uriya Veerendra Murali Krishna [ID], Harsha Avinash Tanti, and Anuradha Chetan Phadake

Abstract—A method is proposed, which uses the digital image processing technique to identify cloud boundaries from scanning Ka-band ($\sim$35.29 GHz) radar imagery dataset. In this method, a cloud is considered as an uninterrupted region of radar echoes with radar reflectivity higher than -34 dBZ and area greater than 3 km^2. The proposed algorithm involves 1) conversion of radar RGB image to grayscale by removing white background and noise, 2) identification of cloud boundaries by canny edge detection, and 3) estimation of cloud cross-section area (CCSA) and cloud top height (CTH) based on the pixel width. This method is effectively applied to Ka-band radar images collected over Mandhardev, a high altitude scanning station in the Western Ghats (WGs), India to derive CTH and CCSA. CTH distribution shows three peaks, one at about 2 km with others at about 7–8 km, and 12 km. The cloud occurrence shows an apparent diurnal variation with a maximum in the afternoon hours while a semidiurnal variation is observed in CCSA. The proposed method shows consistent statistics with Global Precipitation Measurement Ka-band radar observations and thus suitable to build robust cloud climatology over the WGs. Such cloud statistics are essential to validate the representation of clouds in weather and climate models.

Index Terms—Cloud, digital image processing (DIP), diurnal, Ka-band radar, monsoon, Western Ghats (WGs).

I. INTRODUCTION

CLOUDS can modulate the Earth's climate and weather system through their role in the hydrological cycle and radiative energy budget by reflecting, absorbing, and transmitting the solar radiation [1]. The cloud radiative impact depends mostly on cloud bulk properties like its altitude of occurrence, geometrical depth, and spatial distribution. Due to the large spatial and temporal variability, the accurate representation of cloud remains a challenging issue in global climate models and cloud-resolving models [2]. Therefore, it is worth to study the 3-D structure of cloud to improve our understanding on the role of clouds in rainfall and Earth's radiative processes.

Radars operating at millimeter-wavelength are an ideal tool to observe the cloud with high temporal and spatial resolution. The millimeter radars are ideally suited for the detection of weak non-precipitating clouds. The routine measurements of ground-based millimeter radar can provide information on clouds vertical structure and can yield statistics of cloud fraction with altitude, cloud periphery (top and base heights), and radar reflectivity for various types of clouds [3]. With the advent of scanning facilities in the radar system, it is now possible to observe the 3-D structure of clouds within the radar surveillance area.

To understand the typical life cycle of cloud systems during the summer monsoon, Indian Institute of Tropical Meteorology (IITM), Pune, India has deployed mobile Ka-band scanning radar in the mountain range of Western Ghats (WGs) at Mandhardev, India. This radar provides an opportunity to track different stages in the formation of cloud such as initiation, precipitation onset, and dissipation [2]. Such investigation would be helpful to understand the structure, dynamics, and microphysics of monsoon clouds.

Borque *et al.* [2] proposed the cloud identification and tracking algorithm to objectively identify and track clouds for evaluating cloud variability in time and space. The cloud geometrical properties can also be extracted by using digital image processing (DIP) on the weather radar image. DIP technique has successfully been applied to many areas like improving image quality by removing noise [4], medical applications [5], industrial inspection [6], geographic information system [7], human–computer interfaces [8], radar [9], and satellite [10] meteorology. In satellite remote sensing, there are several DIP-based algorithms for cloud detection. For example, some satellites identify cloud based on brightness (radiance) threshold technique where the pixels above a certain threshold value of intensity are considered as a cloud [11]. However, this method sometimes has a caveat of misclassification of clouds due to similar reflectance from other sources (e.g., highly reflective human-made objects, sand in deserts, and snow/ice) [12]. Murtagh *et al.* [13] applied Bayesian technique using statistical pattern recognition based on spatial clustering to perform cloud screening on Moderate Resolution Imaging Spectroradiometer dataset. The fuzzy logic

algorithm was applied to METEOSAT-5 satellite imageries to identify cloud cover [14]. Tseng *et al.* [15] proposed the multi-temporal cloud detection method to identify cloud boundaries. The algorithm determines the cloud periphery from previous image, which defined the cloud. One of the drawbacks of their method is that the time interval of the reference image should be close to the observed image for better accuracy. Zhu and Woodcock [16] proposed a technique Fmask (Function of mask) for cloud and its shadow detection using Landsat imagery. The Fmask utilize top of atmosphere reflectances and brightness temperature to find cloud and cloud shadow mask. Kazantzidis *et al.* [17] presented the k-nearest neighbor algorithm and a binary decision tree for cloud detection from a whole sky imaging system. The method was based on statistical and textural features. Shi *et al.* [18] used deep convolutional neural networks to learn cloud features and generate the cloud probability image. It predicts the cloud region according to the gradient of cloud probability map. Gómez-Chova *et al.* [19] applied statistical machine learning technique to Proba-V satellite images to identify the cloud-contaminated or cloud-free samples. Zhong *et al.* [20] proposed an object-oriented cloud and cloud-shadow matching algorithm for satellite imagery to produce the cloud map. Their method uses the modified automatic cloud cover assessment method based on the relationship between spectral features of an image to create cloud maps and cloud-shadow maps. Deng *et al.* [21] proposed a method for cloud detection in satellite images by first using a simple linear iterative clustering algorithm and defining superpixels. Later, they used natural scene statistic models to distinguish clouds from the surface. Recently, Mahajan and Fataniya [22] summarized different techniques of cloud detection from satellite imagery data.

Although there are several studies [11]–[22] on cloud detection and its classification using image processing, however, there are no extensive studies of DIP application on cloud radar imagery dataset for estimating cloud properties like cloud height and its thickness. In this article, we proposed a simplistic approach of image processing technique to determine the cloud top height (CTH) and cloud area from Ka-band radar images, leading to a few requirements for preprocessing and fast convergence. Development of cloud segmentation algorithm for cloud radar is still an interesting research area. To best of the author's knowledge, this is the first study in the Indian region where CTH and cloud area are estimated from cloud radar images using image processing technique as a tool, which is unexplored and is of interest for the radar community. This article aims to introduce the conceptual and technical framework of a methodology, where DIP technique can be used to analyze the weather radar image (radar images are easily available compared to the raw/processed radar datasets and requires relatively small storage space) and identify the cloud to estimate CTH and cloud cross-section area (CCSA). Cloud area in radar image can be determined based on intensity value (reflectivity) of pixels since cloud pixels will have a higher reflectivity than other pixels. The proposed algorithm works on a platform of Open Source Computer Vision Library (OpenCV) python for postprocessing of radar image. One of the applications of this article lies in utilization of proposed algorithm to build long-term cloud
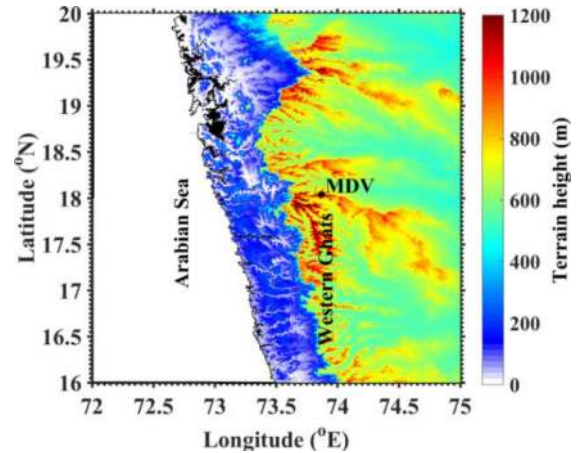

Fig. 1. Topographical map of the Western Ghats of India generated using Shuttle Radar Topography Mission data [23]. Ka-band radar location, Mandhardev (MDV), is shown with a solid black circle.

statistics using Ka-band radar to validate the representation of clouds in numerical models over the mountainous terrain. The structure of the article is as follows. The Ka-band radar system description is in Section II. The methodology is in Section III. Distribution of CTH and CCSA are discussed in Section IV. Section V presents the diurnal variability of CTH and CCSA, and finally, a summary is given in Section VI.

II. SYSTEM DESCRIPTION

A. Ka-Band Radar

The Ka-band radar is deployed at Mandhardev (18.04°N, 73.87°E, ~1.3 km above mean sea level) in the WGs of India. Fig. 1 shows the topography of radar location. The radar used is a scanning radar having dual-polarization facility (linearly polarized in horizontal and vertical directions), manufactured by ProSensing Inc. Amherst, USA. The radar operates at ~35.29 GHz and has a low peak-power klystron transmitter, narrow beamwidth, short pulse lengths, and high-gain antenna. This radar has a minimum detectable reflectivity of −45 dBZ at 5 km range. The antenna is mounted on an elevation-over-azimuth pedestal and designed to rotate continuously in the azimuth axis and a full 180° in the elevation axis—horizon to horizon—with a maximum velocity of 20 deg s^{-1} and a maximum acceleration of 12 deg s^{-2}. The radar and other supporting hardware are mounted on the flatbed truck for mobile applications. Technical specifications of the radar system are provided in Table I and details can be found in Das *et al.* [24].

B. GPM-DPR

The Global Precipitation Measurement (GPM) core observatory was launched in February 2014 and carried the first space-borne dual-frequency precipitation radar (DPR; Ku-band at ~13.6 GHz and Ka-band at ~35.5 GHz). GPM is a nonsolar synchronous satellite inclined at 65° at an altitude of about 407 km and has an orbital period of about 93 min. GPM-DPR provides

TABLE I
CHARACTERISTICS OF THE KA-BAND RADAR SYSTEM

Parameters	Ka-band radar Specification
Frequency	35.29 GHz
Transmitter type	Klystron
Peak Power	2.2 kW
Average Power	~110 W
Antenna aperture	~1.2 m
Antenna gain	49 dB
Beamwidth	0.5°
Pulse length	3.3 μs
Pulse repetition rate	~4960 Hz
Range resolution	~25 m (Pulse compression)

high-resolution 3-D structure of storms which offers a unique opportunity to examine the vertical structure of storms. Details of the GPM-DPR can be found at https://pmm.nasa.gov/gpm. In this article, we used high sensitivity Ka-band scan data to explore the storm top height, which is one of the standard products (GPM Level2A Ka) in GPM-DPR. The storm top height is defined as the altitude of highest range bin that contains precipitating echoes above the minimum thresholds [25].

III. METHODOLOGY

A. Software Used

In this article, the OpenCV library [26] and Python are used for processing the radar imagery data. Along with OpenCV, other libraries such as NumPy, multiprocessing, and matplotlib are used. These libraries are well suited for developing a scientific application where lots of numerical processing, data plotting, and multithreading are required.

B. Preprocessing on the Radar Image

Preprocessing is a method of converting raw data into an appropriate format so that it can be processed further by the main algorithm to achieve the results. The proposed cloud detection method is based on the color separation technique, in which the radar imagery data is considered as an input. The radar image should be in portable network graphics (PNG) or bitmap format due to their lossless compression codecs.

Fig. 2(a) shows the horizon-to-horizon scan of radar reflectivity factor (dBZ) obtained from Ka-band radar measurement on a typical day of August 3, 2016, at 0855 UTC (LT = UTC+0530 h). The colors on image represent different radar echo intensities (reflectivity) measured in dBZ. Clouds are defined in terms of pixels in radar image. Each pixel can be treated as a rectangular area with a predefined value. Here, the length and width of the pixel are 0.01 km and 0.04 km, respectively. The X-Y grid frame in the input image is extracted using a background subtraction method provided by OpenCV. The X-Y grid frame is considered as a closed rectangle and treated as a contour. The extracted X-Y grid frame (specifying the distance from radar along X- and Y-axis in km) is used to find out the dimensions of contour.
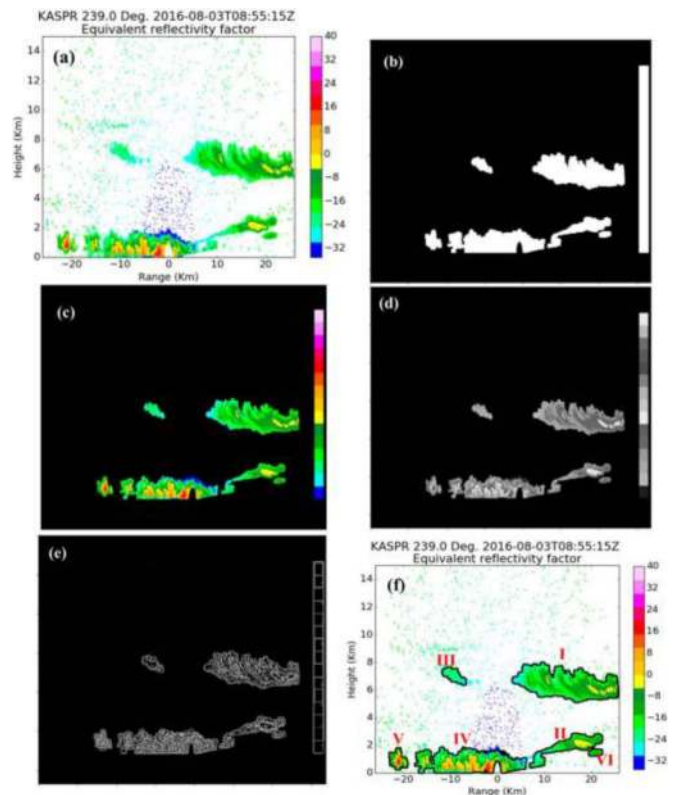

Fig. 2. Different steps in identifying the cloud echoes from cloud radar image. (a) Radar reflectivity (dBZ) during the horizon-to-horizon scan of Ka-band radar. (b) Binary image obtained after converting RGB image to HSV color space. (c) Background is eliminated from the input image. (d) Image converted to grayscale. (e) Cloud echoes identified by using the Canny method of edge detection. (f) Defined clouds with boundaries.

The dimensions of X- and Y-axis in pixels are used to calculate the pixel area and hence used to estimate the CCSA. The CCSA is the horizontal area covered by cloud within the radar horizon-to-horizon scan region. The number of pixels enclosed within the contour can be calculated using image moments. CCSA can be obtained by multiplying the total number of cloud pixels with the area of each pixel. In this article, the area of 1 pixel corresponds to about 0.0004 km^2. The mathematical equation used for CCSA is as follows:

$$\text{CCSA} = \sum_{i,j} x_i \times y_j \qquad (1)$$

where x and y are the width and length of the pixel, respectively, and i and j indicate the number of pixels in the column (along X-axis) and row (along Y-axis), respectively, qualified as a part of the cloud.

CTH is the height of the top-most point of cloud. The CTH is measured in number of pixels that lies between top-most point of cloud and x-axis in that column. By multiplying the total number of pixels of CTH with the pixel length (y) in km gives CTH in km. The CTH can be mathematically expressed as

$$\text{CTH} = \max\left(\sum_{i,j} y_j\right). \qquad (2)$$

The radar reflectivity image in Fig 2(a) contains impulsive noise, which appears as small colored dots on the image. Such noise occurs due to unavoidable factors (e.g., hardware equipment, spectral bins below the signal-noise ratio threshold, celestial radiation wave, clutter, and other interferences). The noise components from the image are filtered by performing erosion and dilation operations. The erosion operation removes random noise present in the picture, whereas dilation operation recovers the information lost during the erosion process. So the combinations of erosion and dilation operations remove small objects from the image and smooth the border of larger objects. It is noted that erosion and dilation will introduce errors in the shape and area of cloud. However, the amount of error present will depend upon the size of erosion and dilation kernel (convolution matrix) used. In this article, we used a square 5 element kernels, which will cause an error of maximum of 4 pixels. Any structure of 4×4 pixels or less will be entirely eroded as the kernel size is 5×5. The error in CTH estimation due to erosion and dilation process is always less than ± 0.05 km (for a 5 element kernel).

For the erosion and dilation operations, the input image should be in binary format. The binary image format can be obtained by converting the radar image (in RGB) into HSV color space with discrete values. A binary image is created by considering the full range of HSV color, as shown in Fig. 2(b). Such conversion technique also supplements the removal of spurious radar echoes such as insect returns or other nonhydrometeor targets. The binary image is then ANDed with background subtracted image to get the background eliminated image [Fig. 2(c)] which is free from the noise. Fig. 2(c) shows the colored blobs of clouds separated from the white background as well as noise.

C. Local Thresholding

The image obtained after removing impulsive noise [Fig. 2(c)] is used to create the mask for radar image in HSV color space using local thresholding technique. The local thresholding procedure is applied to separate the cloud boundary. Here, radar reflectivity factor is used as the threshold parameter. The choice of a threshold value is user-defined because automatic detection may lead to false detection, and also the learning algorithm takes a significant amount of time and memory. In this article, a threshold of -34 dBZ (as the detection capability of IITM's Ka-band radar is about -35 dBZ at 15 km) is considered. When a threshold value is provided, the algorithm produces two masks, namely 1) the entire cloud, and 2) the cloud-free region. By performing high-pass filtering with the threshold value, we can get the cloud mask. These masks are used for error minimization from RGB to grayscale conversion in adaptive thresholding.

D. Adaptive Thresholding

To estimate the area covered by cloud in *X-Y* plane, it is necessary to identify the cloud peripheries. The Canny edge detection method is used to find the cloud boundaries. The parameters for Canny edge detection are source image, resultant image, lower, and upper thresholds for edge detection. The Canny edge detection method is similar to the high-pass filtering of an image in which edges or boundaries between two objects are highlighted by suppressing all other regions with lower spatial frequency [27]. It is well known that the cloud reflectivity changes dynamically, and thus, the color intensities at the border separating cloud and background is different. Therefore, the resultant output will be noisy or may produce inconsistent or broken contour outline due to static canny thresholding method. This issue can be resolved using the dynamic thresholding (adaptive thresholding) method. First, the image is converted from RGB to grayscale. The conversion from RGB to grayscale image can introduce losses in the grayscale image. This can be minimized by superimposing the cloud mask on the grayscale image. The grayscale image is ANDed with the cloud mask created using local thresholding. Fig. 2(d) shows a typical example of converting the RGB image to grayscale. In case, if the radar reflectivity image is available in grayscale, then the grayscale image can directly be superimposed with the cloud mask. Hence, the present algorithm provides the choice of using either RGB or grayscale image as per the availability/convenience. After applying local thresholding, the adaptive thresholding technique is used so that every pixel is separated by a different threshold value depending on its local group [28], [29]. Fig. 2(e) shows the result of adaptive thresholding technique on radar image. This technique will separate the cloud neatly from the image.

E. Cloud Detection and Identification of Cloud Boundaries

The cloud contours are obtained because of the adaptive thresholding. The extreme contour retrieval method is well suited for cloud contour detection as only the outer shape of the cloud plays an essential role during area calculation. Every contour obtained from adaptive thresholding is the boundary of a cloud, and thus these contours can be now treated as a cloud. Fig. 2(f) shows the radar reflectivity image marked with the cloud boundaries obtained using DIP technique. Here, six cloud systems (represented as I, II, III, IV, V, and VI) are identified with well-defined boundaries. The number of pixels enclosed within the contour can be calculated using image moments, and are used to estimate CCSA. The contours with an area smaller than user-defined threshold area are not considered as a valid cloud. Such contours are only highlighted, however not considered for further calculations. In the present study, a threshold value of 3 km^2 is used to calculate CCSA. The area of five cloud systems is about 37.9, 11.9, 3.3, 28.7, and 3.7 km^2, respectively. However, cloud VI is not considered as valid since the calculated area is less than the threshold area of 3 km^2.

To calculate the CTH, a bounding rectangle (rectangle surrounding the cloud) is created based on the weighted mean (centroid) of cloud area. CTH is calculated as the difference between uppermost point on the bounding rectangle and *X*-axis in that column. The CTH for cloud I, II, III, IV, and V are calculated as about 9.8, 2.9, 7.7, 1.8, and 1.8 km, respectively. Fig. 3 shows the workflow of proposed method for the detection of CTH and CCSA from Ka-band radar imagery data.
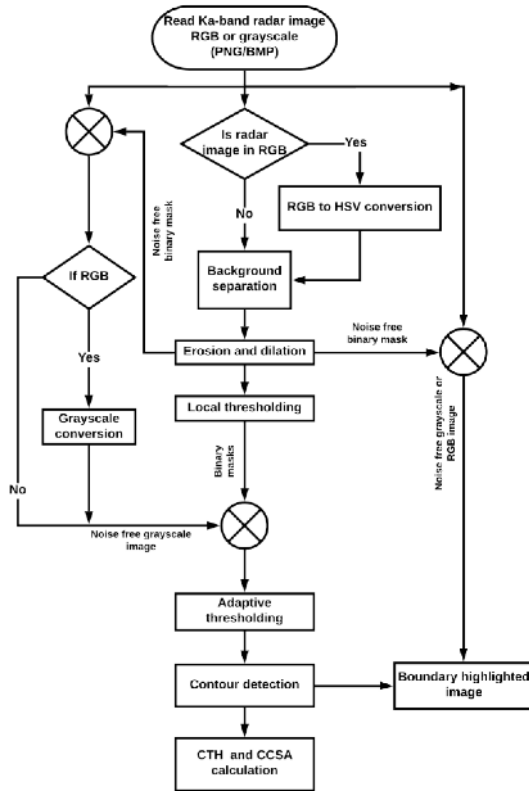
Fig. 3. Flowchart of proposed algorithm for cloud detection from Ka-band radar image.
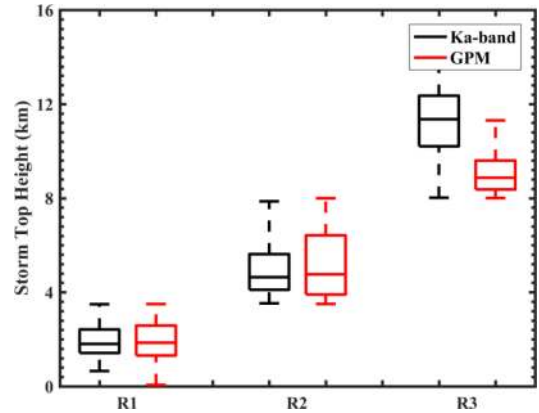

Fig. 4. Box and whisker plot distribution of CTH and storm top height from Ka-band radar, and GPM Ka-band radar, respectively, in different regions. Here, the box represents 25 and 75 percentile of the data, and whiskers show the data within 1.5 times the interquartile range. The horizontal line within the box represents the median value of the distribution.

IV. DISTRIBUTION OF CTH AND CCSA

Investigating the vertical distribution of cloud features like CTH and CCSA is of importance as these parameters can provide a valuable dataset for understanding the role of clouds in modifying the radiative and latent heating rates within the atmosphere [30].

The CTH is derived from horizon-to-horizon scans of Ka-band radar for August–September, 2016. The CTH distribution retrieved from the present algorithm is compared with the GPM Ka-band radar storm top height. The GPM overpass data are considered over the study site during August and September of 2014–2019. For GPM data comparison, we defined a region around radar site to compile statistics from $1° \times 1°$ latitude-by-longitude box centered on radar site. The spatial grid box for comparison is selected in such a way that there is a balance between an area large enough to collect the sufficient number of samples and small enough to be representative of radar site. A total of 7275 and 5336 cloud cases have been identified from Ka-band radar and GPM Ka-band measurements, respectively. Since these comparative evaluations between ground-based radar and GPM Ka-band radar were of accumulation over longer periods rather than snapshot measurements, the results can be compared to examine the variability. For comparison, three different regions are selected: Region 1 (R1: below 3.5 km), Region 2 (R2: 3.5–8 km), and Region 3 (R3: above 8 km). These three regions are chosen to demonstrate the consistency between IITM's Ka-band radar and GPM Ka-band storm top heights below bright band (rain region), mid-level dominated

by mixed-phase, and high-level dominated by ice phase, respectively. Fig. 4 shows the box plot distribution of CTH from Ka-band radar and GPM Ka-band radar in the three regions. Here, all the heights are above the ground level. It is clear that in the regions R1 and R2, the CTH distributions from Ka-band radar are consistent with GPM Ka-band radar. The median value of CTH is nearly the same in both measurements in R1 and R2. The median value of CTH is about 1.8 km (1.9 km), and 4.6 km (4.8 km) in Ka-band (GPM) observations in regions R1, and R2, respectively. However, in region R3, the Ka-band radar shows a larger distribution and higher median value of CTH compared to GPM Ka-band radar measurements. The median value of CTH is about 11.3 km in Ka-band radar, whereas, it is about 8.9 km in GPM Ka-band. This could be due to the lower sensitivity of GPM to weak reflectivities at higher levels. The GPM Ka-band sensitivity is about 12 dBZ [25] and hence, it has a limitation to detect storms above 8 km altitude, compared to ground-based Ka-band radar (sensitivity of about −35 dBZ at 15 km). Even though both the radars (GPM Ka-band and ground-based Ka-band radar) have nearly the same operating frequency, one to one matching between their measurements is quite difficult. This mismatching is due to differences in viewing aspects between space and earth observations, propagation paths, resolution volume size, measurement sensitivity, and time synchronization mismatch [31], [32]. The mean and standard deviation of CTH and storm top height from Ka-band radar and GPM are provided in Table II.

To evaluate the CTH obtained from Ka-band radar in R3, the CTH distributions are compared with cloud profiling radar (CPR) at W-band ($\sim$94 GHz) on-board the National Aeronautics and Space Administration cloud observing satellite (CloudSat) (figure not shown). The CloudSat CPR is a nadir-viewing sun-synchronous satellite, orbiting the Earth's atmosphere at an altitude of about 705 km with an inclination angle of about 98° (refer to http://cloudsat.atmos.colostate.edu). For comparison, the CPR measurements (GEOPROF-LIDAR product) are considered ($1° \times 1°$ latitude-by-longitude box centered on radar site) during August and September of 2006–2010. It is observed

Region	No. of Data		Mean top height (km)		Standard deviation	
	Ka-band	GPM	Ka-band	GPM	Ka-band	GPM
R1	3813	2896	1.95	1.94	0.66	0.81
R2	1484	2132	4.99	5.17	1.16	1.38
R3	1978	308	11.23	9.13	1.46	0.99

Fig. 6. Vertical distribution of CTH at 6 h interval. The magnified profile during 12–18 LT is shown in the inset.
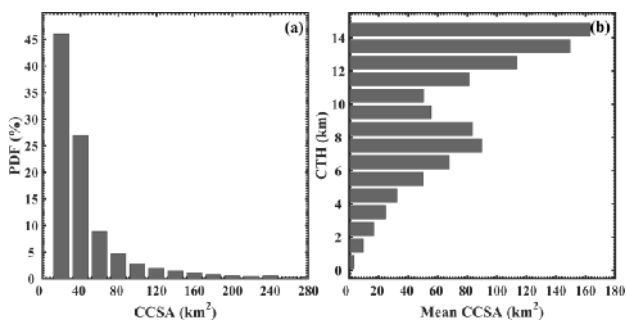

Fig. 5. (a) PDF of CCSA (km^2) for the period August–September, 2016. (b) Distribution of CTH with mean CCSA.

that the median value of CTH is about 11.4 km in CPR data, indicating a good agreement between CPR and ground-based Ka-band radar measurements. It should be noted that despite the different operating frequencies of Ka-band radar and CPR, the CTH distributions are quite consistent. So the DIP method for cloud detection shows the results consistent with the space-borne radar measurements and climatology [33]–[35] indicating the robustness of present algorithm.

Fig. 5(a) shows the histogram of CCSA obtained from Ka-band radar measurements. It is observed that the distribution of CCSA decreases exponentially. The CCSA has maximum distribution below 20 km^2. The distribution of CCSA is within the radar surveillance area. There may be some cases where the cloud is detected by radar; however, it may be extended beyond the radar coverage area. Fig. 5(b) shows the distribution of CTH as a function of CCSA. It is observed that the shallow clouds have limited CCSA (<40 km^2), whereas the taller clouds are widespread. This finding is consistent with Utsav *et al.* [36] that the shallow clouds are isolated pockets of convection forms in the WGs region. The clouds at higher heights are mostly cirrus and/or stratiform-anvil clouds, which usually covers a larger area.

V. DIURNAL CYCLE OF CTH AND CCSA

Understanding the diurnal cycle of clouds is important as they influence the diurnal energy of the Earth's atmosphere and surface. However, investigation of diurnal variation of clouds is limited due to the nonavailability of data with good temporal
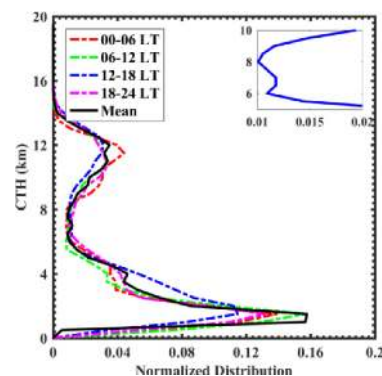
and spatial resolution [37]. The Ka-band radar provides high temporal and spatial resolution data which makes it possible to study the diurnal cycle of clouds. To understand the temporal evolution of CTH on a diurnal timescale, 6 hourly distribution (to ensure a sufficient number of data in each profile) of CTH along with the mean distribution is shown in Fig. 6. Two dominant peaks in the CTH distribution are observed: one at about 2 km and other at about 12 km in the mean CTH. The clouds at 2 km represent the shallow (clouds with tops below 0° isotherms) clouds and at 12 km may be associated with deep convection, anvil or cirrus. Das *et al.* [38] and Utsav *et al.* [36] also observed the dominance of shallow clouds during monsoon in the WGs region. It should be noted that Ka-band radar signals are often attenuated in moderate and heavy rain rates associated with deep clouds, so the actual CTH distribution at higher height may be little higher than estimated [39]. At about 7–8 km, the third peak in CTH distribution is observed, however weak it is. The tri-mode distribution in the CTH is consistent with the climatology of cloud radar data from the Manus ARM site [33] and CloudSat data [34], [35]. The tri-modal distribution is also evident in the radar measurements from Tropical Ocean Global Atmospheric Coupled Ocean-Atmosphere Response Experiment [40]. The CTH distribution shows a similar pattern in each 6 h interval compared to the mean distribution. The CTH distribution increases from ground and reaches its maximum at about 2 km above the ground level. Above this, the distribution decreases with height, and a secondary peak is observed at about 12 km above the ground. Interestingly, a third maximum in the CTH distribution is observed only during 12–18 LT. The third peak is observed at about 7 km above the ground level (magnified profile is shown in the inset). This may be due to the presence of cumulus congestus clouds associated with the solar insolation during day time. The cloud occurrence is maximum at about 2 km during 06–12 LT and minimum during 12–18 LT. This result indicates that the shallow cloud occurrence is maximum in the morning time, representing the oceanic or maritime convection [41], [42]. Whereas at higher levels, about 12 km, the distribution is maximum in mid-night (00–06) h. The midnight peak can occur due to large-scale organized systems, as discussed by *Rao et al.* [43].

Fig. 7(a) shows the composite diurnal pattern of cloud distribution observed by Ka-band radar during August–September,
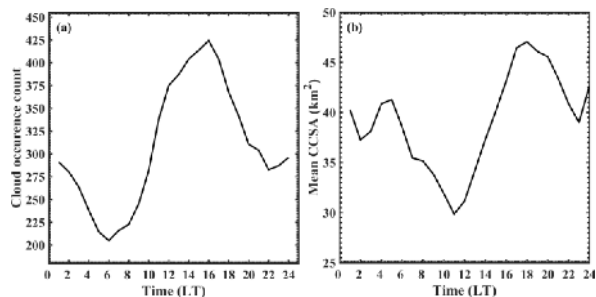
Fig. 7. Composite diurnal cycle of (a) cloud occurrence and (b) mean CCSA (km^2).

2016. The observation shows a clear diurnal cycle centered in the afternoon hours (15–17 LT), in addition to the second peak at mid-night hours (23–24 LT). The afternoon peak is consistent with the diurnal pattern of surface and boundary layer processes. Due to solar insolation and local thermally forced circulations, convection typically initiates over elevated terrain of the WGs during afternoon hours. Ustav *et al.* [36] from ground-based X-band radar observations in the WGs region showed that more number of convective storms occurred during 14–15 LT. Late afternoon peak is in agreement with several other studies using Tropical Rainfall Measuring Mission precipitation data [43], [44] and with regional model study by Flynn *et al.* [45]. The midnight peak can occur due to large-scale organized systems, as discussed by Rao *et al.* [43]. Our finding of mid-night peak also supports the results of Utsav *et al.* [36] where they found a second peak in vertically integrated liquid (liquid water content within the storm) in the mid-night hours apart from the highest peak in the evening hours (16–17 LT). Using Cloud-Aerosol Transport System lidar data during summer, Noel *et al.* [46] observed the vertical cloud profiles over different regions in the globe. They found a similar bi-modal distribution of clouds in 15–30°N latitude. The diurnal cycle of clouds observed in this article also supports the results obtained by Lang *et al.* [47] and Johnson *et al.* [48] during the North American Monsoon Experiment. Fig. 7(b) shows the diurnal cycle of CCSA. Interestingly, CCSA has a semidiurnal pattern with the first peak at about 17–18 LT and a second peak at about 04–05 LT. It is observed that the morning minimum in CCSA ($\sim$11 LT) lags the minimum of cloud occurrence ($\sim$06 LT) by 5 h. Whereas, the night minimum in CCSA ($\sim$23 LT) lags the minimum of cloud occurrence ($\sim$22 LT) by 1 h.

VI. Summary

This study proposed a method to identify cloud boundaries and estimate CTH and CCSA by utilizing DIP technique on scanning Ka-band radar imagery data. The algorithm is based on OpenCV and Python software. The horizon-to-horizon scans of Ka-band radar image (in PNG format) is considered. The binary masking and converting the image to grayscale removes the white background and noise from the image. Further, the Canny edge detection and adaptive thresholding techniques are used to identify and extract the boundary of each cloud layer. A cloud layer is determined based on a region having a contiguous

set of pixels exceeding the reflectivity of -34 dBZ and area greater than 3 km^2.

The main application of this method lies in examining the CTH and cloud horizontal distribution in 2-D space, which is defined as CCSA. Two months (August–September, 2016) of scanning Ka-band radar data are analyzed with DIP algorithm to determine CTH and CCSA. The distribution of CTH showed two climatological peaks: one in the lower troposphere at about 2 km and other in the upper troposphere at about 12 km. In addition, a third peak in mid-troposphere at about 7–8 km is also evident in the CTH distribution. The CTH distribution obtained from the proposed algorithm matches well with the storm top height measurements of GPM Ka-band radar. The CCSA shows an exponential distribution with a majority of clouds cover less than 20 km^2. The diurnal cloud variation shows an afternoon peak, however, a semidiurnal variation is observed in the CCSA.

The proposed DIP method provides a framework to identify CTH and CCSA in the cloud radar imagery data without involving complicated numerical techniques. The observational evidence of CTH and CCSA distribution can be helpful to deduce the skill of models (numerical weather prediction and general circulation model), in reproducing the observed cloud distribution over complex mountainous terrain.

References

[1] K. N. Liou, *Radiation and Cloud Processes in the Atmosphere*. New York, NY, USA: Oxford Univ. Press, 1992.

[2] P. Borque, P. Kollias, and S. Giangrande, "First observations of tracking clouds using scanning ARM cloud radars," *J. Appl. Meteorol. Climatol.*, vol. 53, no. 12, pp. 2732–2746, Sep. 2014.

[3] P. Kollias, E. E. Clothiaux, M. A. Miller, B. A. Albrecht, G. L. Stephens, and T. P. Ackerman, "Millimeter-wavelength radars: New frontier in atmospheric cloud and precipitation research," *Bull. Amer. Meteorol. Soc.*, vol. 88, no. 10, pp. 1608–1624, Jan. 2007.

[4] J. S. Lee, "Digital image enhancement and noise filtering by use of local statistics," *IEEE Trans. Pattern Anal. Mach. Intell.*, vol. PAMI-2, no. 2, pp. 165–168, Mar. 1980.

[5] G. Dougherty, *Digital Image Processing for Medical Applications*. New York, NY, USA: Cambridge Univ. Press, 2009.

[6] W. Osten, *Optical Inspection of Microsystems*. Boca Raton, FL, USA: CRC Press, 2007.

[7] J. R. Jensen and K. Lulla, "Introductory digital image processing: A remote sensing perspective," *Geocarto Int.*, vol. 2, no. 1, Mar. 1987, Art. no. 65.

[8] T. E. Hutchinson, K. P. White, W. N. Martin, K. C. Reichert, and L. A. Frey, "Human-computer interaction using eye-gaze input," *IEEE Trans. Syst. Man Cybern.*, vol. 19, no. 6, pp. 1527–1534, Nov./Dec. 1989.

[9] M. W. Merritt, "Automated detection of microburst wind-shear for terminal doppler weather radar," in *Proc. Digit. Image Process. Vis. Commun. Technol. Meteorol.*, Jan. 1987, pp. 61–68.

[10] V. Lakshmanan, K. Hondl, and R. Rabin, "An efficient, general-purpose technique for identifying storm cells in geospatial images," *J. Atmos. Ocean. Technol.*, vol. 26, no. 3, pp. 523–537, Mar. 2009.

[11] C. M. Wittenbrink, G. G. Langdon Jr., and G. Fernàndez, "Feature extraction of clouds from GOES satellite data for integrated model measurement visualization," *IS&T/SPIE Symp. Electron. Imag., Image Video Process.*, vol. 2666, pp. 212–222, Mar. 1996.

[12] J. H. Jeppesen, R. H. Jacobsen, F. Inceoglu, and T. S. Toftegaard, "A cloud detection algorithm for satellite imagery based on deep learning," *Remote Sens. Environ.*, vol. 229, pp. 247–259, Aug. 2019.

[13] F. Murtagh, D. Barreto, and J. Marcello, "Decision boundaries using bayes factors: The case of cloud masks," *IEEE Trans. Geosci. Remote Sens.*, vol. 41, no. 12, pp. 2952–2958, Dec. 2003.

[14] A. Ghosh, N. R. Pal, and J. Das, "A fuzzy rule based approach to cloud cover estimation," *Remote Sens. Environ.*, vol. 100, pp. 531–549, Feb. 2006.

[15] D.-C. Tseng, H.-T. Tseng, and C.-L. Chien, "Automatic cloud removal from multi-temporal SPOT images," *Appl. Math. Comput.*, vol. 205, pp. 584–600, Nov. 2008.

[16] Z. Zhu and C. E. Woodcock, "Object-based cloud and cloud shadow detection in Landsat imagery," *Remote Sens. Environ.*, vol. 118, pp. 83–94, Mar. 2012.

[17] A. Kazantzidis, P. Tzoumanikas, A. F. Bais, S. Fotopoulos, and G. Economou, "Cloud detection and classification with the use of whole-sky ground-based images," *Atmos. Res.*, vol. 113, pp. 80–88, Sep. 2012.

[18] M. Shi, F. Xie, Y. Zi, and J. Yin, "Cloud detection of remote sensing images by deep learning," in *Proc. IEEE Int. Geosci. Remote Sens. Symp.*, Jul. 2016, pp. 701–704.

[19] L. Gómez-Chova, G. Mateo-García, J. Munoz-Marí, and G. Camps-Valls, "Cloud detection machine learning algorithms for PROBA-V," in *Proc. IEEE Int. Geosci. Remote Sens. Symp.*, Jul. 2017, pp. 2251–2254.

[20] B. Zhong, W. Chen, S. Wu, L. Hu, X. Luo, and Q. Liu, "A cloud detection method based on relationship between objects of cloud and cloud-shadow for chinese moderate to high resolution satellite imagery," *IEEE J. Sel. Top. Appl. Earth Observ. Remote Sens.*, vol. 10, no. 11, pp. 4898–4908, Nov. 2017.

[21] C. Deng, Z. Li, W. Wang, S. Wang, L. Tang, and A. C. Bovik, "Cloud detection in satellite images based on natural scene statistics and gabor features," *IEEE Geosci. Remote Sens. Lett.*, vol. 16, no. 4, pp. 608–612, Apr. 2019.

[22] S. Mahajan and B. Fataniya, "Cloud detection methodologies: Variants and development—A review," *Complex Intell. Syst.*, vol. 6, pp. 251–261, Jul. 2020.

[23] T. G. Farr *et al.*, "The shuttle radar topography mission," *Rev. Geophys.*, vol. 45, May 2007, Art. no. RG2004.

[24] S. K. Das, Y. Kisan Kolte, U. V. Murali Krishna, S. M. Deshpande, A. K. Jha, and G. Pandithurai, "Estimation of layer-averaged rain rate from zenith pointing Ka-band radar measurements using attenuation method," *IEEE J. Sel. Top. Appl. Earth Observ. Remote Sens.*, vol. 12, no. 9, pp. 3178–3183, Aug. 2019.

[25] K. Toyoshima, H. Masunaga, and F. A. Furuzawa, "Early evaluation of Ku- and Ka-band sensitivities for the global precipitation measurement (GPM) dual-frequency precipitation radar (DPR)," *SOLA*, vol. 11, pp. 14–17, Feb. 2015.

[26] J. Howse, *OpenCV: Computer Vision With Python*. Birmingham, U.K.: PacktPublishing, 2013.

[27] J. Canny, "A computational approach to edge detection," *IEEE Trans. Pattern Anal. Mach. Intell.*, vol. PAMI-8, no. 6, pp. 679–698, Nov. 1986.

[28] R. C. Gonzalez and R. E. Woods, *Digital Image Processing*, 2nd ed. London, U. K.: Pearson Education, 2002.

[29] J. Sauvola and M. Pietikainen, "Adaptive document image binarization," *Pattern Recognit.*, vol. 33, no. 2, pp. 225–236, Feb. 2000.

[30] J. Wang, W. B. Rossow, and Y. Zhang, "Cloud vertical structure and its variations from a 20-yr global rawinsonde dataset," *J. Climate*, vol. 13, no. 17, pp. 3041–3056, Sep. 2000.

[31] S. M. Bolen and V. Chandrasekar, "Methodology for aligning and comparing spaceborne radar and ground-based radar observations," *J. Atmos. Ocean. Technol.*, vol. 20, no. 5, pp. 647–659, May 2003.

[32] S. K. Das, U. V. M. Krishna, Y. K. Kolte, S. M. Deshpande, and G. Pandithurai, "Assessment of ground-based X-band radar reflectivity: Attenuation correction and its comparison with space-borne radars over the Western Ghats, India," *Earth Space Sci.*, vol. 7, 2020, Art. no. e2019EA000861.

[33] S. Hollars, Q. Fu, J. Comstock, and T. Ackerman, "Comparison of cloud-top height retrievals from ground-based 35 GHz MMCR and GMS-5 satellite observations at ARM TWP manus site," *Atmos. Res.*, vol. 72, no. 1, pp. 169–186, 2004.

[34] E. M. Riley and B. E. Mapes, "Unexpected peak near −15°C in cloudsat echo top climatology," *Geophys. Res. Lett.*, vol. 36, no. 9, pp. L09818-1–L09818-5, 2009.

[35] S. K. Das, R. B. Golhait, and K. N. Uma, "Clouds vertical properties over the northern hemisphere monsoon regions from CloudSat-CALIPSO measurements," *Atmos. Res.*, vol. 183, pp. 73–83, Jan. 2017.

[36] B. Utsav, S. M. Deshpande, S. K. Das, and G. Pandithurai, "Statistical characteristics of convective clouds over the Western Ghats derived from weather radar observations," *J. Geophys. Res. Atmos.*, vol. 122, no. 18, pp. 10,10–50,76, Sep. 2017.

[37] J. W. Bergman and M. L. Salby, "Diurnal variations of cloud cover and their relationship to climatological conditions," *J. Climate*, vol. 9, no. 11, pp. 2802–2820, Nov. 1996.

[38] S. K. Das, M. Konwar, K. Chakravarty, and S. M. Deshpande, "Raindrop size distribution of different cloud types over the Western Ghats using simultaneous measurements from micro-rain radar and disdrometer," *Atmos. Res.*, vol. 186, pp. 72–82, Apr. 2017.

[39] Q. Zhou *et al.*, "Cloud-base and cloud-top heights determined from a ground-based cloud radar in Beijing, China," *Atmos. Environ.*, vol. 201, pp. 381–390, Mar. 2019.

[40] R. H. Johnson, T. M. Rickenbach, S. A. Rutledge, P. E. Ciesielski, and W. H. Schubert, "Trimodal characteristics of tropical convection," *J. Climate*, vol. 12, pp. 2397–2418, 1999.

[41] T. Nitta and S. Sekine, "Diurnal variation of convective activity over the tropical western pacific," *J. Meteorol. Soc. Jpn. Ser. II*, vol. 72, no. 5, pp. 627–641, 1994.

[42] C. Sui, K. Lau, Y. N. Takayabu, and D. A. Short, "Diurnal variations in tropical oceanic cumulus convection during TOGA COARE," *J. Atmos. Sci.*, vol. 54, pp. 639–655, Mar. 1997.

[43] T. N. Rao, K. Saikranthi, B. Radhakrishna, and S. V. Bhaskara Rao, "Differences in the climatological characteristics of precipitation between active and break spells of the indian summer monsoon," *J. Climate*, vol. 29, no. 21, pp. 7797–7814, Jul. 2016.

[44] S. Shige, Y. Nakano, and M. K. Yamamoto, "Role of orography, diurnal cycle, and intraseasonal oscillation in summer monsoon rainfall over the western ghats and myanmar coast," *J. Climate*, vol. 30, no. 23, pp. 9365–9381, Sep. 2017.

[45] W. J. Flynn, S. W. Nesbitt, A. M. Anders, and P. Garg, "Mesoscale precipitation characteristics near the Western Ghats during the indian summer monsoon as simulated by a high-resolution regional model," *Quart. J. Roy. Meteorol. Soc.*, vol. 143, no. 709, pp. 3070–3084, Oct. 2017.

[46] V. Noel, H. Chepfer, M. Chiriaco, and J. Yorks, "The diurnal cycle of cloud profiles over land and ocean between 51°S and 51°N, seen by the CATS spaceborne lidar from the international space station," *Atmos. Chem. Phys.*, vol. 18, pp. 9457–9473, Jul. 2018.

[47] T. J. Lang, D. A. Ahijevych, S. W. Nesbitt, R. E. Carbone, S. A. Rutledge, and R. Cifelli, "Radar-observed characteristics of precipitating systems during NAME 2004," *J. Climate*, vol. 20, no. 9, pp. 1713–1733, May 2007.

[48] R. H. Johnson, P. E. Ciesielski, T. S. L'Ecuyer, and A. J. Newman, "Diurnal cycle of convection during the 2004 North American monsoon experiment," *J. Climate*, vol. 23, no. 5, pp. 1060–1078, Mar. 2010.

Subrata Kumar Das received the M.Sc. degree in physics from Guru Ghasidas University, Bilaspur, India, in 2002, and the Ph.D. degree in physics from National Central University, Chung-Li, Taiwan, in 2011.

He worked as Visiting Lecturer and Project Fellow with Guru Ghasidas University, Bilaspur, from 2002 to 2004 and 2004 to 2005, respectively. He was among the team members to develop a portable 3-D scanning Lidar system during his doctoral research for which Gold Medal in the "Third NCU Instrument Innovation Competition-2009" was awarded. He has been a Research Scientist with the IITM, Ministry of Earth Sciences, Pune, India, since March 2011. His research interests include the understanding of various atmospheric dynamical processes that drive the regional and global Earth systems, with a primary focus on radar meteorology, precipitation physics, cloud dynamics, characterization of optical properties of aerosols, and tropopause dynamics.

Dr. Das was the recipient of URSI Young Scientist Award-2011, University Meritorious Award, and many best paper awards.

Pranjal Prasad Joshi was born on 3rd December 1995, in Kolhapur, India. He received the Diploma degree in electronics & telecommunication from Government Polytechnic, Kolhapur, India, in 2014, and the B.Eng. degree in electronics & telecommunication from the SPPU (formerly Pune University), Pune, India, in 2017.

He was with the Bharat Electronics Limited as a Probationary Engineer, in 2017. He is currently working in development and engineering of defense electronics including artillery fuzes and batteries. His research interests include artificial intelligence and machine learning, image processing, embedded systems, development of new products, as well as streamlining the production process.

Harsha Avinash Tanti was born on 24th February 1995, in Rishra, Hooghly, India. He received the B.Sc. (Honors) degree in electronics from Vidyasagar College, University of Calcutta, Kolkata, India, in 2016, and the M.Sc. degree in electronics from the SPPU (formerly Pune University), Pune, India, in 2018.

He was a Teaching Assistant with the SPPU, from 2018 to 2019. He was with IIT Indore as a Scientific Technician, in 2019. He is currently a Research Scholar with IIT Indore and working on Low-frequency Astronomy from Space. His research interests include signal processing, image processing, machine learning, deep learning, polarimetry, and RF design & engineering.

Rohit Satish Kokitkar received the B.Eng. degree in electronics & telecommunication from the SPPU (formerly Pune University), Pune, India, in 2017.

Anuradha Chetan Phadake received the B.E. and M.E. degree in electronics from Walchand College of Engineering, Sangli, India, in 1993 and 1995, respectively, and the Ph.D. degree in electronics and telecommunication engineering from Savitribai Phule Pune University, Pune, India, in 2016.

She is currently working as an Associate Professor with the School of Electronics and Communication Engineering, Dr. Vishwanath Karad Maharashtra Institute of Technology World Peace University, Pune, India. She has authored two books and published and presented several papers in indexed journals and conferences. Her research interests include image processing, machine learning, and embedded system design.

Dr. Phadake was the recipient of Ideal Teacher Award given by Maharashtra Academy of Engineering & Education Research, in 2011.

Uriya Veerendra Murali Krishna received the master's degree in physics from Sri Venkateswara University, Tirupati, India, in 2007 and the Ph.D. degree in physics from Yogi Vemana University, Kadapa, India, in 2016.

He is currently a Project Scientist with the Indian Institute of Tropical Meteorology, Pune, India. His research interests include remote sensing of the atmosphere, understanding the characteristics of orographic precipitation using radar and satellite observations, and quantitative precipitation estimation from radar measurements.